

Impact Behavior of Dense Debris Flows Regulated by Pore-Pressure Feedback

Dongri Song^{1,2} , Xiaoqing Chen^{1,2} , Hamed Sadeghi³ , Wei Zhong^{1,2}, Huawei Hu⁴, and Wei Liu^{1,2} 

¹Institute of Mountain Hazards and Environment, Chinese Academy of Sciences, Chengdu, China, ²University of Chinese Academy of Sciences, Beijing, China, ³Department of Civil Engineering, Sharif University of Technology, Tehran, Iran, ⁴Chengdu NewPro Technology Co., Ltd., Chengdu, China

Key Points:

- Comprehensive experimental measurements reveal the impact-pressure characteristics of dense and dilute debris flows
- A time-dependent creeping mode is observed for dense debris-flow impact, which is regulated by the pore-pressure feedback in the impact process
- A tentative phase diagram is proposed for dense and dilute debris-flow impact

Supporting Information:

Supporting Information may be found in the online version of this article.

Correspondence to:

X. Chen,
xqchen@imde.ac.cn

Citation:

Song, D., Chen, X., Sadeghi, H., Zhong, W., Hu, H., & Liu, W. (2023). Impact behavior of dense debris flows regulated by pore-pressure feedback. *Journal of Geophysical Research: Earth Surface*, 128, e2023JF007074. <https://doi.org/10.1029/2023JF007074>

Received 18 JAN 2023
Accepted 30 NOV 2023

Author Contributions:

Conceptualization: Xiaoqing Chen
Data curation: Dongri Song, Wei Zhong
Investigation: Xiaoqing Chen, Hamed Sadeghi, Huawei Hu
Methodology: Dongri Song, Huawei Hu
Resources: Wei Zhong
Supervision: Xiaoqing Chen
Validation: Dongri Song, Hamed Sadeghi
Writing – original draft: Dongri Song

Abstract The impact dynamics of dilute debris flows (typically volumetric solid fractions < 50%) have been extensively investigated within the framework of hydraulics. For dense debris flows, the impact mechanisms have been poorly studied. From a geotechnical viewpoint, the feedback between granular dilatancy and pore-pressure response may play an important role in the dense debris-flow regime. In this study, the impact behavior of dense and dilute debris flows in an instrumented flume is analyzed. The basal stresses (normal/shear stresses, pore-fluid pressure) and impact pressure on a rigid barrier are measured. A time-dependent creeping mode is observed for the impact process of slow-moving dense debris flows, which cannot be accurately estimated using current debris-flow load models. At the grain scale, this macroscopic creeping mode is a result of the feedback between granular dilatancy and pore-pressure response. This feedback can be further characterized by examining the timescales associated with pore-pressure generation and dissipation. The regulation of pore-pressure feedback on basal shear stress, impact load, and state of static deposit is revealed. Finally, a tentative phase diagram is proposed for dense and dilute debris-flow impact. The proposed framework complements the theory for debris-flow impact loads.

Plain Language Summary The destructive power of fast-moving debris flows has been continuously emphasized in the scientific literature and the public media. However, a substantial portion of debris flows are actually slow-moving and seem less destructive, even if their real destructiveness remains unknown. We conducted flume experiments of dilute (low solid-fraction) and dense (high solid-fraction) debris flows impacting a rigid obstacle. Our findings highlight the effect of the interplay between granular void change and interstitial fluid-pressure evolution on the mobility and impact behavior of debris flows. Especially for dense debris flows, the high solid fraction results in an ultralow rate of pore-pressure dissipation and a high basal shear stress. For these flows, the impact is reflected in the stoppage of the material and its creeping deformation. In addition, it may not be possible to accurately estimate the impact load using fast-flow load models, indicating that existing models for estimating the destructive power of these flows should be cautiously considered when assessing and mitigating the associated risks.

1. Introduction

The impact load is used for quantifying the destructive power of debris flows, and is one of the key parameters for designing debris-resisting structures (Hübl et al., 2009; Hungr et al., 1984; Kwan, 2012). An effective theoretical model needs to reflect the key processes and mechanisms of debris-flow impact, which are usually revealed through field observations (Hu et al., 2011; Nagl et al., 2022) or well-controlled flume experiments (Scheidl et al., 2013; Song, Chen, et al., 2021; Zanuttigh & Lamberti, 2006). Efforts have been made during the past few decades to reach some consensus on debris-flow impact behavior. From a hydraulic standpoint, the impact load of debris flow obeys Froude scaling (Armanini et al., 2020; Vagnon & Segalini, 2016). The kinetic behavior and impulse-load characteristics of entrained boulders have been revealed (Johnson et al., 2012; Ng et al., 2021). National or regional guidelines have been established or recently updated to reflect the current understanding of debris-flow impact, including guidelines of Austria (ASI, 2011, 2013), China (CAGHP, 2018), Japan (NILIM, 2016a, 2016b), and Hong Kong SAR (GEO, 2020).

Current research mainly focuses on fast-moving debris flows, which can be characterized by a Froude number higher than unity. The destructive power (inertial force) of fast-moving debris flows is visually recognizable. A typical case of channelized debris-flow impact of the Jiangjia Ravine (China), triggered by heavy rainfall and

stream runoff, is demonstrated in Movie S1. “Viscous-like” slow-moving debris flows can also be observed in the branch gully of Jiangjia Ravine (Movie S2) and in the Xiaogangjian Gully of the 2008 Wenchuan earthquake area (Movie S3). These flows are characterized by a walking pace or slower velocity. Slow-moving debris flows are more frequent on open hillslopes, with a transition from slope failure to flowslide (Iverson et al., 1997). In this context, we do not deliberately differentiate “flow” from “flowslide” (Hung et al., 2014). The impact behavior of slow-moving debris flows (with $Fr < 1$) has rarely been investigated since they are characterized by less inertial force and are recognized as less destructive.

The grain-scale solid-fluid interaction, which fundamentally governs the macroscopic flow and impact behavior of debris flow, can be represented by its volumetric solid fraction (Fang et al., 2022). The debris-flow solid fraction typically ranges from 40% to higher than 60% (Hung et al., 2014). As the solid fraction increases, the resistance to flow increases accordingly (Pierson, 2005) and the macroscopic motion seems “viscous” (time-dependent, Iverson, 2005). Iverson and George (2014) emphasized how the initial solid fraction influences the mobility of flow-type landslides. More specifically, a drastic change in mobility can result from small differences in the initial solid fraction but a drastic response in pore-fluid pressure.

Apart from geologists, scientific problems related to debris flows have attracted researchers from both hydraulic and geotechnical communities. The flow-like nature of debris flows can be well described using hydraulic models (Armanini et al., 2020; Chanson, 2004). The evolution of the granular stress state and its coupling with pore-fluid pressure can be described within the framework of critical-state soil mechanics (Iverson et al., 1997; Wood, 1990). Due to the nearly liquefied characteristics of low solid-fraction (typically <50%) debris flows, the impact loads can be estimated using hydraulic models (Armanini et al., 2020; Kong et al., 2022a, 2022b; Liu et al., 2019), and the majority of current debris-flow impact experiments are within this range of solid fraction (<50%). The particle-contact effective stress within this range is negligible (Song et al., 2022, even not measured in most cases). Therefore, the critical question is, “with weak effective stress, is the low solid-fraction debris-flow impact process fluid-dominated or solid-dominated?” In contrast, for dense debris flows (solid fraction >50%), the particle-contact frictional effective stress dominates (Bowman et al., 2010), and the granular assembly tends to dilate under shear (Guazzelli & Pouliquen, 2018; Pailha et al., 2008), which further affects the pore-pressure evolution. However, the dynamics of dense debris flows, especially how pore-pressure feedback regulates impact behavior, remain largely unknown.

This paper first introduces the existing physics-based models for debris-flow impact loads. Different from the current debris-flow experiments with low solid fraction, this study specifically focuses on the impact behavior of dense debris flows. Through novel and dedicated measurements of basal stresses (normal/shear stresses, pore-fluid pressure) and two-phase (solid-phase and fluid-phase) impact pressure on a rigid barrier, the target is to shed light on the effects of pore-pressure feedback on the impact process. Finally, a phase diagram is proposed to unify the impact behavior of a wide spectrum of flow types.

2. Theoretical Considerations

2.1. Estimation of a Debris-Flow Impact Load

Currently, two distinct impact models have been recognized for estimating a debris-flow impact load, that is, the vertical jet model (Armanini et al., 2020) and the momentum jump model (Albaba et al., 2018; Faug, 2020). Both models obey the conservation of momentum along the flow direction. As a typical open-channel problem, the impact load is composed of both flow inertia and static load and thus is a function of the Froude number.

The vertical jet model is an abstract of the formation of violent jet-up along the barrier face, denoting a 90° deflection of the momentum from the incoming flow direction (see Figure 1a). The impact load per unit width F can be expressed as (Armanini et al., 2020; Kyburz et al., 2022; Salm, 1967; Voellmy, 1955)

$$\begin{aligned}
 F &= \rho v^2 h + \frac{1}{2} k \rho g h^2 \cos \theta \\
 &= \rho v^2 h \left(1 + \frac{k}{2Fr^2} \right) \\
 &= \frac{1}{2} \rho g h^2 \cos \theta (2Fr^2 + k)
 \end{aligned} \tag{1}$$

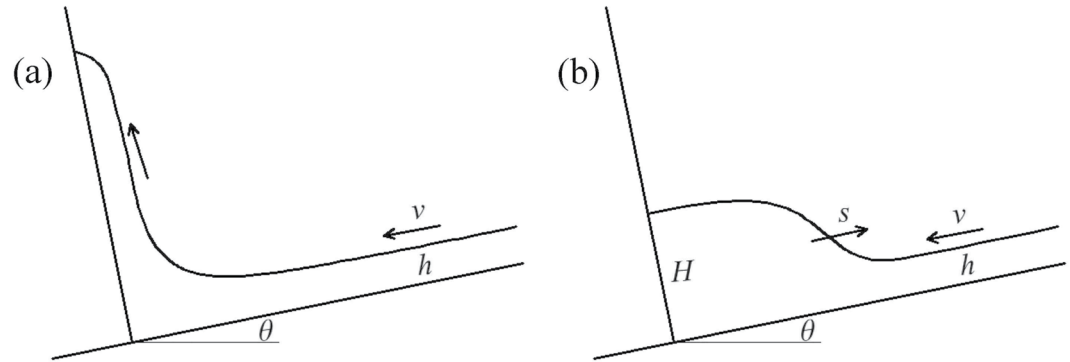


Figure 1. Schematic illustration of debris-flow impact models: (a) vertical jet mode and (b) momentum jump mode (Song, Chen, et al., 2021).

where ρ is bulk density (kg/m^3); θ is slope inclination ($^\circ$); v is velocity (m/s); h is incoming-flow depth (m); and k is coefficient of earth pressure of incoming flow upon impacting the barrier, which is regulated by the degree of liquefaction λ

$$\lambda = \frac{p}{\sigma} \quad (2)$$

where p is pore-fluid pressure (kPa) and σ is total normal stress (kPa). The force resulting from inertia, normalized by the force imposed by earth's gravitational field, is known as the Froude number (Faug, 2015)

$$Fr = \frac{v}{\sqrt{gh \cos \theta}} \quad (3)$$

For the design of debris-resisting barriers, when the impact load F is expressed in the form of inertial force $\rho v^2 h$, $1 + \frac{k}{2Fr^2}$ is equivalent to a dynamic pressure coefficient α , and the design approach is called the hydrodynamic approach ($F = \alpha \rho v^2 h$). When F is expressed in the form of gravitational force $\frac{1}{2} \rho g h^2 \cos \theta$, $2Fr^2 + k$ is equivalent to a static pressure coefficient β , and the design approach is called the hydrostatic approach ($F = \frac{1}{2} \beta \rho g h^2 \cos \theta$).

The momentum jump model considers the momentum exchange due to the reflected wave (jump interface) in the upstream direction (see Figure 1b). The impact load per unit width F can be expressed as

$$\begin{aligned} F &= \rho v h (v + s) + \frac{1}{2} k \rho g h^2 \cos \theta \\ &= \frac{1}{2} k_H \rho g H^2 \cos \theta \\ &= \frac{1}{2} \rho g h^2 \cos \theta \left[k_H \left(\frac{H}{h} \right)^2 \right] \end{aligned} \quad (4)$$

where $s = \frac{hv}{H-h}$ is velocity of the reflected wave; H is deposition height at the barrier (Figure 1b); and k_H is coefficient of earth pressure of the deposit. The advantage of this momentum jump model is that it relies only on the incoming-flow properties (flow depth h and velocity v) to predict the impact load F and deposition height H . The analytical solution for H/h and the derivation of the momentum jump model can be found in Albaba et al. (2018).

Theoretically, the impact load with the momentum jump mode is higher than that of the vertical jet since the momentum due to the reflected wave is explicitly considered in the impact load. However, the results from controlled experiments demonstrate that the difference between these two analytical models is even smaller than the discreteness of impact loads (Song, Chen, et al., 2021). Note that existing experimental studies mainly focus on fast-moving dilute flows (solid fraction < 50%), which are generally characterized by Froude numbers higher than 3. The flow and impact behavior of slow-moving dense flows remain uninvestigated and serves as the key target of this study.

Table 1
Test Program and Flow Regime of Incoming Flow

Test ID	Solid fraction (%)	Viscosity η (Pas)	Bulk density ρ (kg/m ³)	Gate uplift (mm)	Froude number Fr	Degree of liquefaction λ_{flow}	Regime based on Courrech du Pont et al. (2003)
Dry granular	–	Air	1,524.0	120	2.83	–	–
60–1	60	0.001	2,010.6	Dam break	2.17	0.18	Inertial
60–10		0.01	1,979.6	Dam break	0.11	–0.27 ^a	Viscous
60–100		0.1	1,924.0	Dam break	0.59	0.18	Viscous
55–1	55	0.001	1,847.0	100	5.59	0.59	Inertial
55–10		0.01	1,909.4	100	3.66	0.77	Inertial
55–100		0.1	1,944.3	100	0.36	0.87	Viscous
50–1	50	0.001	1,770.0	100	5.02	0.80	Viscous
50–10		0.01	1,839.4	100	5.06	0.94	Viscous
50–100		0.1	1,878.2	100	4.18	0.88	Viscous

^aNegative pore pressure due to dilation and surface tension.

2.2. Framework of Granular Dilatancy Under Shear

The dilatancy of granular material is controlled by its stress state. Under quasistatic shear conditions, dense granular material dilates toward its critical state when it is sheared under a relatively low effective stress (confining pressure), while loose granular material tends to contract toward the critical state (Wood, 1990). For flowing debris, the stress state includes not only the effective stress but also particle-collisional stress $\rho_s \delta^2 \dot{\gamma}^2$ and fluid-viscous stress $\dot{\gamma} \eta$. In other words, granular dilatancy is also affected by the physical processes of particle collision and fluid viscous drag. The framework proposed by Iverson and George (2014), which quantifies the contribution of the shear rate to granular dilatancy, is adopted to calculate the dilatancy under shear

$$\tan \psi = m - \frac{m_{\text{crit}}}{1 + \sqrt{N}} \quad (5)$$

$$N = \frac{\dot{\gamma} \eta}{\rho_s \dot{\gamma}^2 \delta^2 + \sigma_e} \quad (6)$$

where ψ is dilatancy angle ($^\circ$); m is volumetric solid fraction and m_{crit} is the critical-state solid fraction (0.58 for mono-sized glass beads; Gravish & Goldman, 2014) at which the granular material would not dilate or contract under shear; ρ_s is density of solid phase (kg/m³); δ is representative particle diameter (m); $\sigma_e = \sigma - p$ is particle-contact effective stress (kPa); and $\dot{\gamma}$ is average shear rate (1/s). Due to the effect of sidewall friction, the velocity at the sidewall is lower than that at the centerline of the flow (Jop et al., 2005). In this study, the shear rate is deduced based on the flow regime and their corresponding velocity profiles. Specifically, given that particles are fully mixed with the fluid (no sedimentation), $\dot{\gamma} = 3v/2h$ for the viscous flow profile and $\dot{\gamma} = 5v/3h$ for the Bagnoldian (inertial) flow profile (Cassar et al., 2005; Song, Zhou, & Chen, 2021). To distinguish the relative dominance of viscous and inertial (particle collision) effects, the “viscous” and “inertial” flow regimes follow the definition of Courrech du Pont et al. (2003). A description of the flow regimes is detailed in Text S1 of the Supporting Information S1 and summarized in Table 1.

3. Methodology

Debris-flow impact with a volumetric solid fraction of 60% and dry granular-flow impact are investigated. Combined with the impact with solid fractions of 55% and 50% by Song, Chen, et al. (2021), this study covers a wide spectrum of geophysical flows, including debris flows with varying solid fractions and debris avalanches.

3.1. Model Setup

A flume was adopted to investigate the impact of debris flow on a rigid barrier (Figure 2b). The flume has one 5 $^\circ$ downstream section and one 25 $^\circ$ upstream section. The upstream end of the flume is an isolated storage container

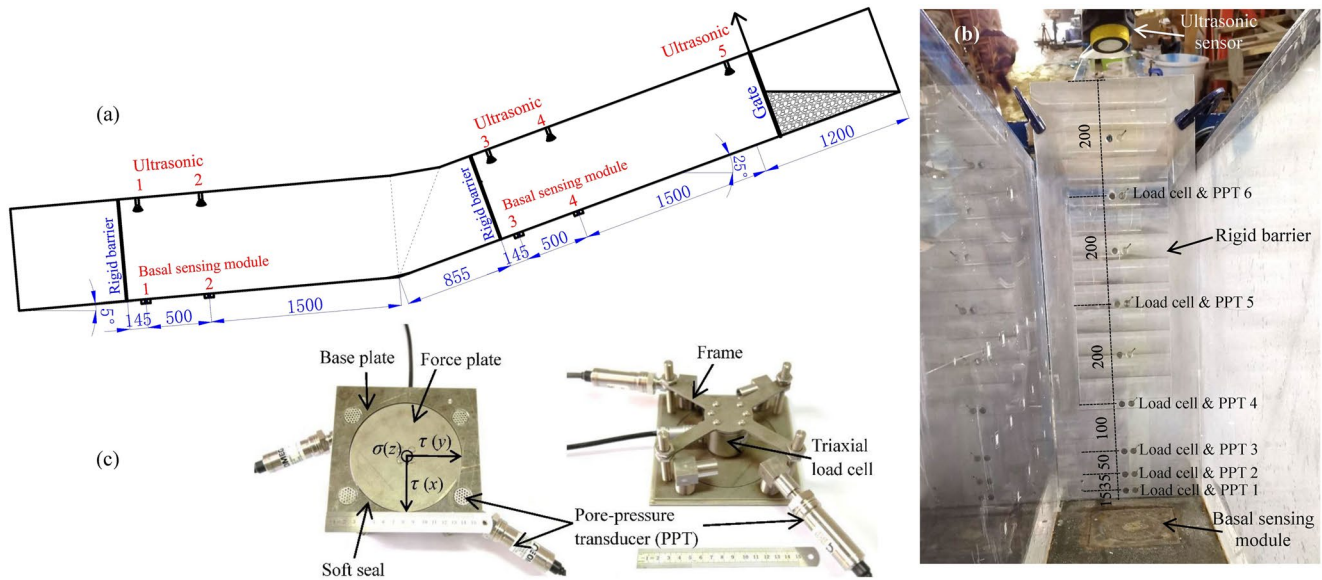


Figure 2. Experimental setup and instrumentation: (a) flume setup with a rigid barrier on 25° section (this study) or 5° section; (b) rigid barrier (looking downstream) for measurement of the total impact pressure and pore-fluid impact pressure; and (c) basal sensing modules for measurement of the normal/shear stresses and pore-fluid pressure. All dimensions are in mm.

with an uplift gate for debris material release. The width of the flume is 300 mm. The sidewall is made of acrylic glass so that the trajectory can be measured using particle image velocimetry (PIV) technique. The flume bed is roughened using 0.6 mm diameter spherical glass beads, which are also used as the solid phase of the debris flow in this study.

An 800 mm high, 300 mm wide, and 10 mm thick aluminum barrier was erected perpendicular to the flume bed (Figures 2a and 2b). To simulate the impact of slow-moving dense flows (60%) and dry granular flow, a barrier was installed 2,145 mm downstream of the gate (in the 25° upstream section). To simulate the impact of fast-moving dilute flows (55% and 50%), a barrier is installed 5,145 mm downstream of the gate in the 5° downstream section (Song, Chen, et al., 2021). The purpose of different test setups (inclination, distance from release, and manner of gate uplift) for varying solid fractions is to ensure that the incoming flows prior to impact are steady and have a low Froude number close to that of natural debris flows.

3.2. Instrumentation

The normal and shear stresses at the flume bed are measured using basal sensing modules (triaxial load cell, model number: LH-SZ-02, maximum range: 50 N, accuracy: $\pm 0.1\%$ BSL, Figure 2c) distributed along the channel. Pore-fluid pressure is measured using a pore-pressure transducer (PPT, model number: OMEGA PX409, maximum range: 6.9 kPa/34.5 kPa, accuracy: $\pm 0.08\%$ BSL, Figure 2c). The open end of the PPT is filled with a glycerol-water mixture to effectively transmit the fluid pressure. The open end of the PPT is further covered by a 0.4 mm steel mesh, which isolates the force induced by the solid phase. Flow depth is measured using ultrasonic sensors (model number: BANNER U-GAGE T30UXUA, range: 0.1–1.0 m, resolution: 0.1% of distance) directly above the basal sensing modules.

To measure the impact pressure of the solid phase, 12 mm diameter miniature load cells (model number: TML CLS-10NA/CLS-20NA, accuracy: 0.5% RO) are embedded in the rigid barrier with their surfaces flush with the barrier face (Figure 2b). The total impact pressure is calculated based on the measured force and the surface area of the load cell. The lower part of the barrier is intensively instrumented since the impact-pressure gradient is much steeper. Pore-pressure transducers (PPTs) are installed in conjunction with miniature load cells (Figure 2b) so that the contribution of the solid phase to the overall impact load can be clarified. Typical calibration data of the above sensors are summarized in Figure S2 of the Supporting Information S1. A high-speed camera (PHOTRON FASTCAM Mini WX50) with a resolution of 1,280×1,024 pixels is set alongside the flume. With a field of view of 800 mm, the captured image has a resolution of 1.6 pixel/mm. The velocity field of the granular-fluid

mixtures can be deduced using PIV technology (GeoPIV software) at the sidewall. By tracking the image texture of patches (20×20 pixels in this study) of the original image in subsequent frames, PIV analysis calculates the displacement field via a series of images taken over the course of deformation (Sanvitale & Bowman, 2016). The displacement field is then converted to the velocity field through a known time interval between images. Two video cameras were also adopted to capture the impact kinematics alongside and over the barrier.

3.3. Debris-Flow Materials

It is common practice to adopt analog materials in debris-flow research (Fang et al., 2022) since the interactions between graded soil particles and non-Newtonian slurries are rather complicated and still lie on the frontier of granular physics. This study simplifies natural debris flows as mixtures of mono-sized glass beads (0.6 mm, $2,540 \text{ kg/m}^3$) and a Newtonian fluid (glycerol-water solution). By adding 2% black glass beads of the same diameter, the solid texture can be substantially enhanced for PIV analysis. A Newtonian fluid (glycerol-water solution) is used for the fluid phase.

3.4. Test Program and Procedure

Volumetric solid fractions of debris flow are set as 60%, 55%, and 50%, and fluid dynamic viscosities are set as 0.1, 0.01, and 0.001 Pa·s (water as the fluid phase) to cover the typical viscosity of natural debris flows. One dry granular flow impact, with the same granular material as the two-phase debris flow, was also carried out for comparison. As revealed in the test results, the dynamic behavior of dry granular flows shares some remarkable characteristics with that of dense debris flows. The bulk density ranges from 1,524.0 to $2,010.6 \text{ kg/m}^3$. The test program is summarized in Table 1. To determine the Froude flow regime of unsteady flows, frontal flow velocity and peak flow depth were adopted.

The volume for debris material is set to 0.05 m^3 . To prevent solid-fluid separation prior to release, the two-phase mixtures remain well-mixed by using a helical mixer. In an attempt to generate moving flows with constant depth, the debris material is released at a constant gate opening of 100 mm (for 50% solid fraction flow) and 120 mm (for dry granular flow). For those with solid fractions higher than 55%, the dam-break approach is adopted. The sampling rate of the data acquisition system is 1,000 or 100 Hz (depending on flow velocity), and frame rate of the high-speed camera is 250 fps.

4. Basal Shear Stress Regulated by Granular Dilatancy and Pore-Pressure Feedback

From a geotechnical viewpoint, the basal shear stress of debris flows is mainly contributed by the particle-contact effective stress of the solid phase, and the effective stress is further controlled by the pore-pressure response. The pore pressure, in turn, is regulated by the contraction or dilation behavior of the solid phase. Typical basal stress measurements of incoming flow for tests dry granular, 60–100, 55–100, and 50–100 are shown in Figure 3. Owing to the low solid fractions of tests 55–100 and 50–100, the granular skeleton tends to contract under gravity. To quantify the effect of contraction, the hydrostatic pore pressure is deduced from the measured flow depth, that is, $\rho_f g h \cos \theta$, where ρ_f is density of fluid phase. The positive excess pore pressure (difference between measured pore pressure and hydrostatic pore pressure) indicates that the measured pore-fluid pressure is close to the normal stress and that the fluid phase bears most of the debris-flow total weight (Figures 3c and 3d). With increasing solid fraction to 60%, the granular skeleton dilates, and the measured pore-fluid pressure stays below the hydrostatic pore pressure (Figure 3b). The degree of liquefaction for the two-phase debris flows is summarized in Table 1. The negative correlation between the solid fraction and the degree of liquefaction is clear. However, the relationship between pore-pressure feedback and granular dilatancy needs further quantification.

All the dry granular flow and two-phase debris flows record substantial shear stress for the incoming flows. The shear stresses of tests dry granular, 60–100, and 55–100 are sustained throughout the process (Figure 3a–3c), denoting the contribution of the endured particle-contact effective stress. For test 50–100, the formation of a vertical jet along the barrier face (Figure 5d) and its subsequent fall-back cause the debris to move upstream. The corresponding shear stress at this stage becomes negative (Figure 3d), denoting shear stress in the upstream direction.

Based on the framework of granular dilatancy under shear (Section 2.2), the relationship between excess pore pressure (normalized by hydrostatic pore pressure $\rho_f g h \cos \theta$) and granular dilatancy is plotted in Figure 4a. Despite the discreteness of the data, the negative correlation between the dilatancy and excess pore pressure is

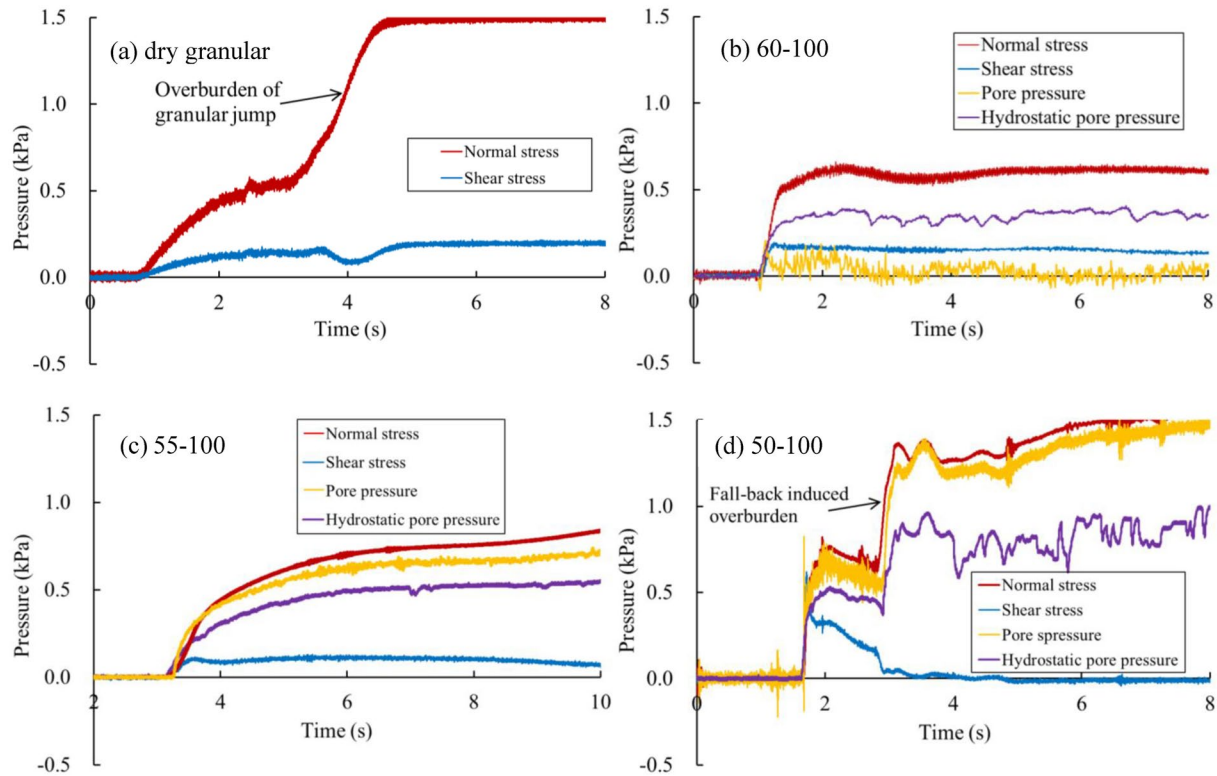


Figure 3. Measured basal normal stress, shear stress, and pore-fluid pressure of incoming flows: (a) dry granular at basal sensing module 4; (b) 60–100 at basal sensing module 4; (c) 55–100 at basal sensing module 2; and (d) 50–100 at basal sensing module 2. $t = 0$ s denotes the release of debris material from the gate.

clear. Furthermore, it appears that the response of pore pressure to dilatancy is nonlinear, and the negative excess pore pressure is more sensitive to particle dilation.

As the pore pressure directly regulates the particle-contact stress, the relationship between the apparent friction coefficient (ratio between shear and normal stresses) and excess pore pressure is shown in Figure 4b. The data are fitted in different combinations, that is, three 60% solid-fraction points as a group (purple line), six 60% + 55% solid-fraction points as a group (red line), and all 60% + 55% + 50% solid-fraction points as a group (blue line). A general decreasing trend is observed for increasing excess pore pressure, which is consistent with the theory of soil mechanics. However, with the addition of low solid-fraction data points, the relationship becomes less significant, indicating that other physical processes start to contribute to the basal shear stress. Recent research has revealed the contribution of visco-collisional stresses to the macroscopic basal shear stress, especially for those with negligible effective stress (Amarsid et al., 2017; Chen et al., 2023; Song, Zhou, & Chen, 2021). This may form the main source for the basal shear stress of dilute debris flows.

The degree of liquefaction indicates the overall efficiency of converting the potential energy to kinetic energy. As the degree of liquefaction approaches unity, the energy consumption by effective-stress friction becomes negligible, and a higher kinetic energy (Froude number) is achieved (Figure 4c). Thus, an appropriate estimation of the degree of liquefaction is essential for estimating the flow regime and impact load. In the following sections, we further refer to the pore-pressure feedback regulated by granular dilatancy and the state of liquefaction to explain the dynamic and static responses on the rigid barrier.

5. Impact Load and Pore-Pressure Response

5.1. Impact Kinematics

Typical impact processes for tests dry granular, 60–100, 55–100, and 50–100 are shown in Figure 5. PIV analysis was carried out to deduce the velocity field and to further discern the mode of interaction with the barrier (momentum jump, vertical jet, or others). Test dry granular is characterized by a typical granular jump, with

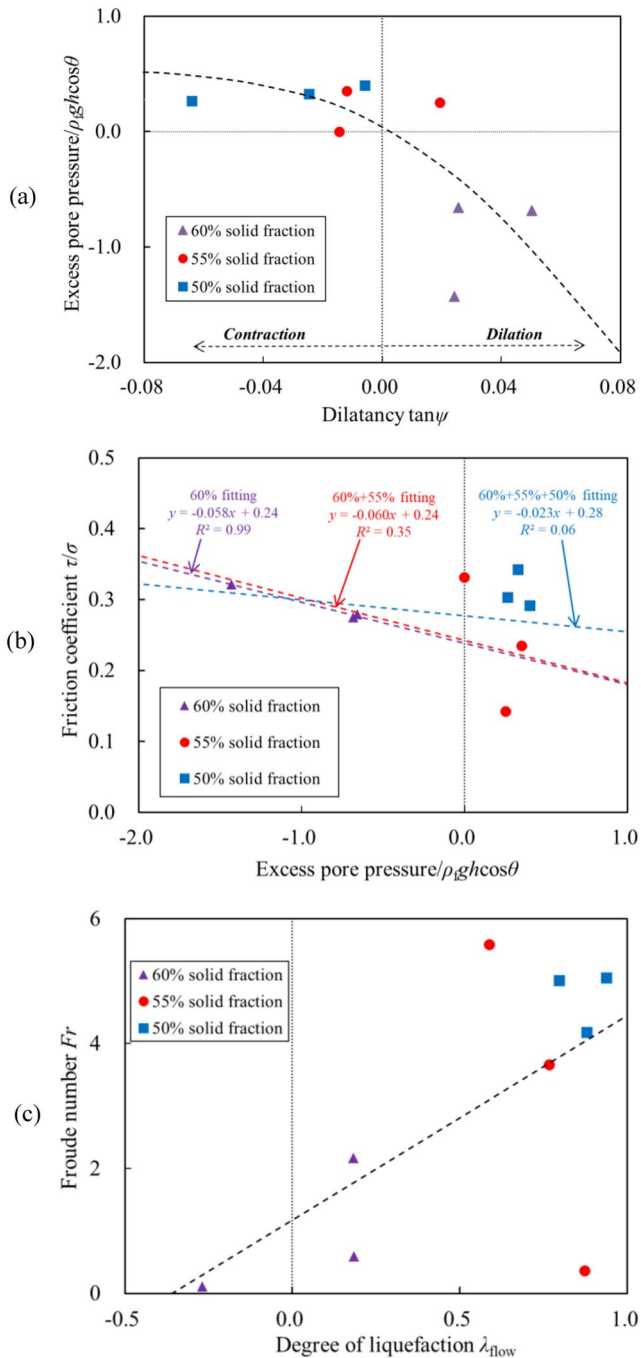


Figure 4. Relationship between (a) excess pore pressure and particle dilatancy; (b) apparent friction coefficient and excess pore pressure; and (c) Froude regime and degree of liquefaction.

the velocity of incoming flow gradually attenuating to zero across the jump. As the supply of incoming flow proceeds, the jump interface moves in the upstream direction with speed s ($t = 2.00, 2.60,$ and 3.00 s, Figure 5a; Movie S4), which can be well described by the momentum jump theory (Equation 4). The particles after the jump gradually readjust to form a slope with a repose angle of the glass beads. The impact process of test 50–100 can be well described by the vertical jet mode (Equation 1), where the incoming flow is deflected vertically (Figure 5f; Movie S5), without further momentum exchange with the barrier.

The impact processes of tests 60–100 and 55–100, however, do not simply lie in between as a transition from momentum jump to vertical jet. For test 60–100, due to the negative excess pore pressure, the measured shear stress is actually higher than that of the dry granular flow (Figures 3a and 3b). As a result, the velocity is one order of magnitude lower. This reflects the effect of negative pore-pressure feedback on the movement of dense debris flows. The flow front approaches the barrier base, and subsequent flow gradually pushes the previous deposit to increase its height at the barrier face. In this process, the subsequent flow cannot override the previous deposit and interact with the barrier (Figures 5b and 5c; Movie S6). The whole “impact” process is quasistatic and takes approximately 60 s to complete (within seconds for dry granular and dilute flows, Figure 8).

This apparent time-dependent “creeping” deformation, under relatively constant debris depth, is actually controlled by granular dilatancy and pore-pressure feedback (Iverson, 2005). Note that “creep” in mechanics may have a different meaning. The term “creep” is adopted here to describe this time-dependent behavior, only out of respect to the long-established use of this term in the geomorphology literature (Hung et al., 2014). For dense debris flows, granular dilatancy enhances the voids between particles and causes a drop in pore-fluid pressure; the pore-fluid pressure in turn restrains further deformation of the granular skeleton through enhanced effective stress. The degree of regulation induced by pore-pressure feedback on the granular deformation depends on the rate of seepage (pore-pressure dissipation, see Section 7.3), which makes the macroscopic impact behavior time-dependent or “viscous.”

5.2. Impact Pressure and Pore-Pressure Response

The impact-pressure time history of the momentum jump mode reflects the gradual accumulation of dry granular flow at the barrier (Figure 6a). As the jump interface detaches from the barrier, the recorded impact pressure remains constant, denoting that the impact load at the barrier is dominated by a static load. The gradual increase in total impact pressure reflects the creeping mode of dense debris flows upon impact (Figures 6b and 6c). The key difference between tests 60–100 and 55–100 is that the negative excess pore pressure (as shown by the green lines) is sustained in the impact process of test 60–100. While for test 55–100, as the shear rate diminishes in the deposit, shear dilatancy further decreases (Equations 5 and 6), and the degree of liquefaction approaches unity. The dynamic response of test 50–100 reflects the violent jet-up process. As expected for liquefied flows, the pore pressure fully follows the impulse characteristics of the total impact pressure (Figure 6d), rendering a macroscopic fluid-like behavior of dilute debris flows.

Dense debris flows in this study remain saturated with negative excess pore pressure (test 60–100, Figure 6b). This means that there is higher shear strength in the creeping process, and the shear stress during the creeping

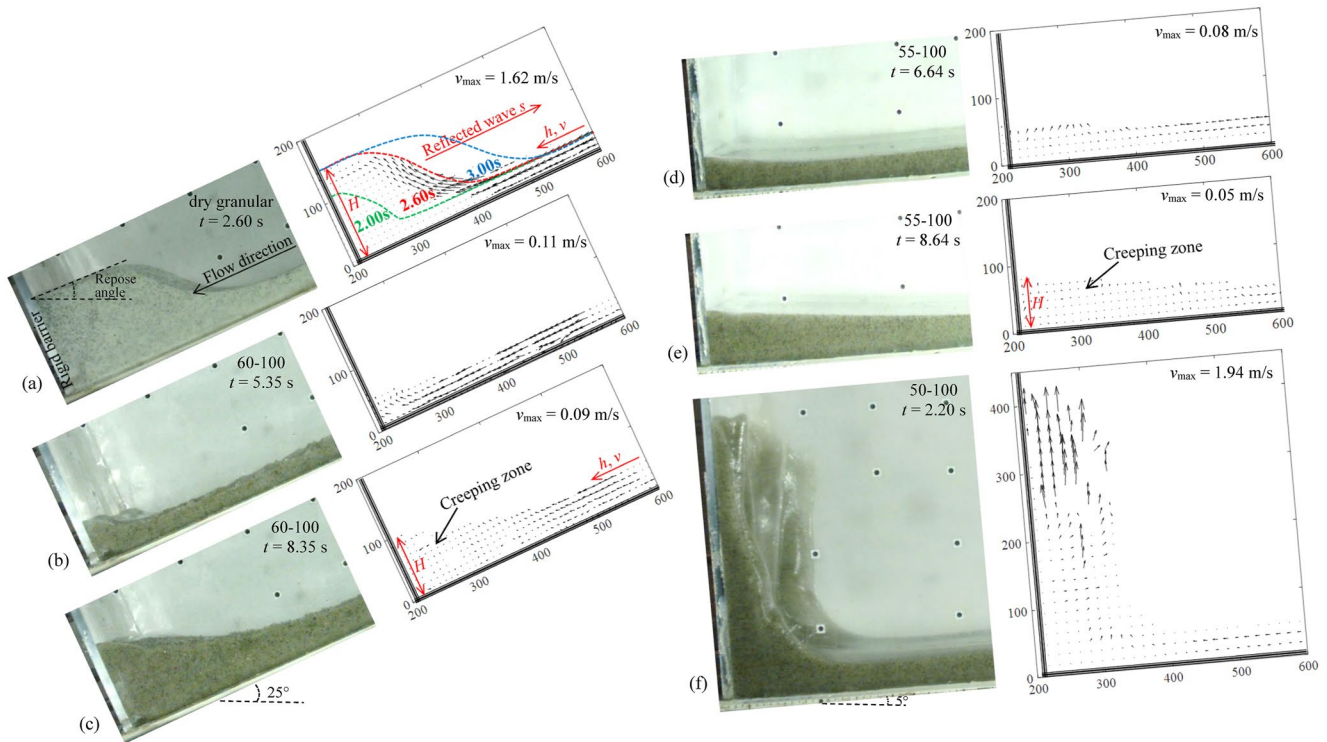


Figure 5. Observed impact kinematics and corresponding PIV analysis: (a) dry granular, $t = 2.60$ s, stratified deposition of $t = 2.00$ and 3.00 s is also shown to demonstrate the deposition pattern upon reaching the repose angle; (b) 60–100, $t = 5.35$ s; (c) 60–100, $t = 8.35$ s; (d) 55–100, $t = 6.64$ s; (e) 55–100, $t = 8.84$ s; and (f) test 50–100, $t = 2.20$ s. Linear dimensions in mm. $t = 0$ s denotes the release of debris material from the gate.

process can be reserved in the final deposit (stress-history dependent behavior). We check the state of deposit through the static load on the barrier in Section 5.4.

5.3. Pressure Profile and Impact Load

The pressure profile along the barrier height further reveals the difference between dense and dilute debris flows. The pressure profiles at the moment of the typical impact stage, for example, initial impact, impact load rise, and static load (Figure 7), are shown. The pressure profiles of test dry granular and 60–100 show pressure drops near the barrier base (Figures 7a and 7b), which are caused by the arching effect of the granular material (see the inset diagram of Figure 7a). Within the arching zone, the force chains are weaker than those of the arch, leading to a lateral pressure drop at the barrier base. Note that granular arches form only when there is substantial particle-contact stress. Therefore, the pressure profiles are linear for test 55–100 (Figure 7c), because the debris approaches liquefied in the deposition process. Above the arching zone, the pressure profiles of tests dry granular and 60–100 are linear, corroborating the dominance of the static load.

The pressure distribution of the vertical jet mode (test 50–100) is highly nonlinear, with the peak pressure concentrated on the lower portion of the barrier. As revealed by Song, Chen, et al. (2021), the trajectory of debris in the jet is parallel to the barrier face (Figure 5f). In this region, there is no more momentum exchange with the barrier. The pressure profile becomes linear in the final deposit (green line in Figure 7d).

The pressure distribution can be further integrated along the barrier height to obtain the total impact load (Figure 8). The impact load of dry granular flow reaches a plateau immediately after the granular jump height reaches its maximum and moves upstream (Figure 5a). The loading process of test 60–100 is quite slow, which depends on the particle readjustment and pore-pressure feedback in the creeping process. The loading process of test 55–100 was slightly quicker. As shown in Figure 6c, the deposit of test 55–100 gradually liquefies (total normal stress close to the pore-fluid pressure), thus the regulation by pore pressure is relatively weak. The impact-load time history of test 50–100 is characterized by a sharp impulse. This corresponds to the jet-up and fall-back processes of fully liquefied flow.

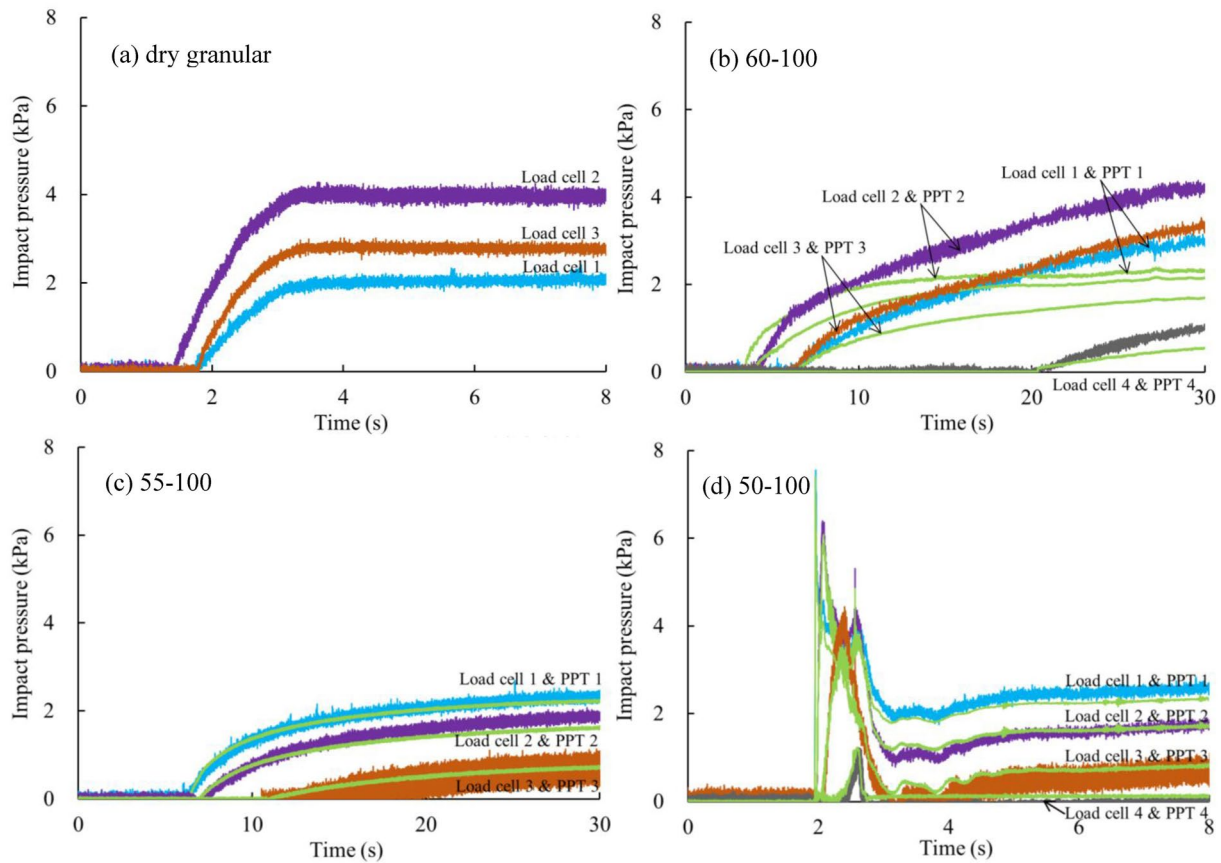


Figure 6. Total impact pressure and their corresponding pore-pressure response (in green) along barrier height: (a) dry granular, no pore-pressure response for dry flow; (b) 60–100, due to arching effect, the total pressure at barrier base (load cell 1) is lagged behind its corresponding pore pressure; (c) 55–100; and (b) 50–100. Note the difference in timescales in the *x*-axis.

The impact loads of this study, together with those of Song, Chen, et al. (2021) and Armanini et al. (2020), are plotted against the Froude number (Figure 9). Since the final deposition height H of the creeping flows is several times the incoming-flow depth h , the impact load at the moment of one-time flow depth h at the barrier is adopted for comparison. The impact loads are further normalized by the static load $0.5\rho gh^2 \cos \theta$ (Equations 1 and 4). Although the data points collected here are from well-controlled experiments, substantial discreteness is observed. This explains why the fitted curves of the F - Fr relationship are reported in varying forms (Kwan, 2012; Song et al., 2018). Nevertheless, the data points generally follow the prediction of theoretical models (Figure 9). A sufficient factor of safety is needed for the design of countermeasures to compensate for the uncertainty of natural debris flows. Based on the interaction patterns with the barrier, the vertical jet mode and momentum jump mode can be clearly distinguished (see Figure 5) with a threshold of $Fr = 3$ –4. Two of the creeping-mode data points are higher than the prediction of the momentum jump model. The load of the creeping mode cannot be well described by existing load models (Equations 1 and 4).

5.4. State of Static Deposits of Dense Flows

With a special focus on the impact loads of dense flows, in the range $Fr < 3$ –4, the impact loads (mainly static) of dry granular flow and 60% fraction flows (within the dashed ellipse) are systematically higher than those of the theoretical lines and other measured data with a low solid fraction (Figure 9). On the premise of significant particle-contact stresses regulated by pore-pressure feedback, we postulate that this deviation is induced by the passive state of debris deposits (deposit being compressed horizontally; Sovilla et al., 2010).

The static loads of the final deposits, rather than the impact loads at one-time flow depth, are plotted against the loads from active/passive Coulomb earth pressure theory (Figure 10). For the coefficient of earth pressure in

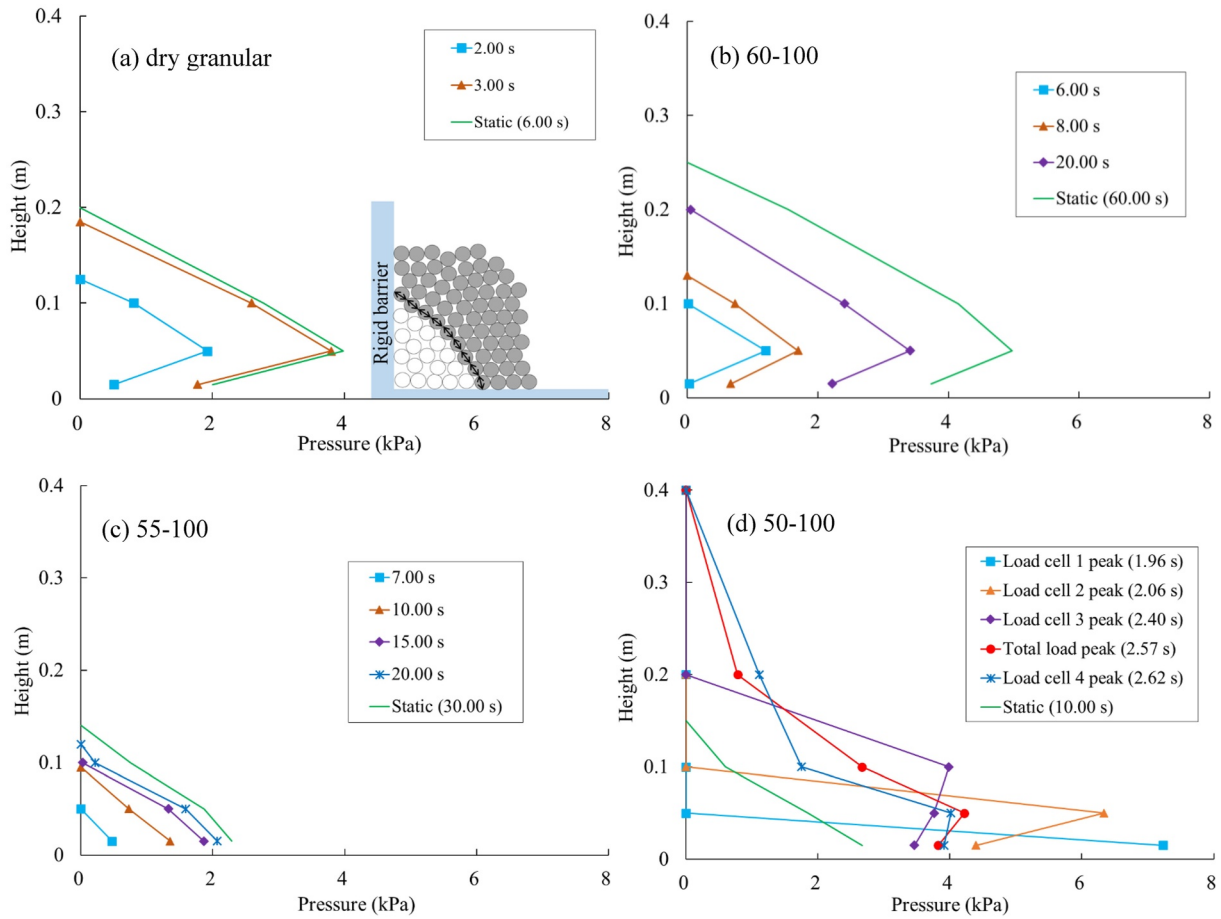


Figure 7. Pressure profile of (a) dry granular, inset diagram showing granular arch at barrier base; (b) 60–100, (c) 55–100, and (d) 50–100.

the final deposit k_H , it is related to the coefficient of earth pressure for dry granular flow k_s and regulated by the degree of liquefaction λ_{deposit} , which can be obtained from the basal sensing modules (Figure 11; Table 2)

$$k_H = k_s(1 - \lambda_{\text{deposit}}) + \lambda_{\text{deposit}} \quad (7)$$

Depending on the state of the granular material, k_s could be the coefficient of active earth pressure k_a or the coefficient of passive earth pressure k_p (Iverson & George, 2019). As λ_{deposit} reaches unity, k_H also approaches unity.

Data points lying around each dashed line fitted from the origin denote that they are in a similar state, and the data points on the diagonal line indicate that the state of debris is in the active failure mode (Figure 10). In this way, the state of static debris with different absolute values can be compared. Note that the earth pressure at rest is difficult to accurately determine for a sloping ground with an inclined retaining barrier. However, it is certain that the at-rest state of granular material (with a coefficient of earth pressure at rest of approximately 0.5) is close to the active state (lower limit of active earth pressure coefficient of 0.2) and far from the passive state (upper limit of passive earth pressure coefficient of 5 or even higher). Therefore, the states of both dry granular flow and 60% fraction flow are close to the passive state, and this is especially obvious for the 60% fraction flows (Figure 10), where the deposit is pushed against the barrier by the subsequent flow (Figures 5b and 5c).

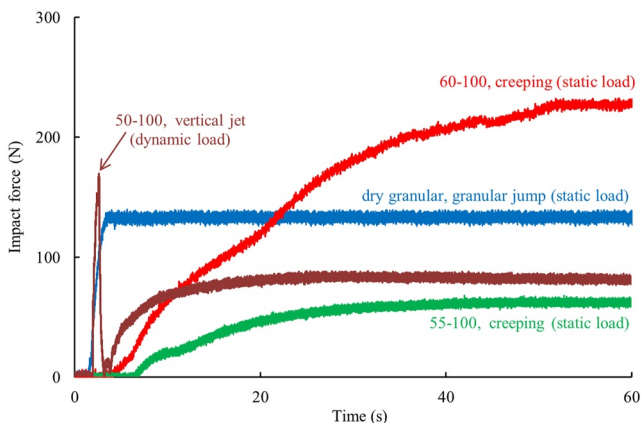


Figure 8. Three typical impact-load time histories: creeping, granular jump, and vertical jet.

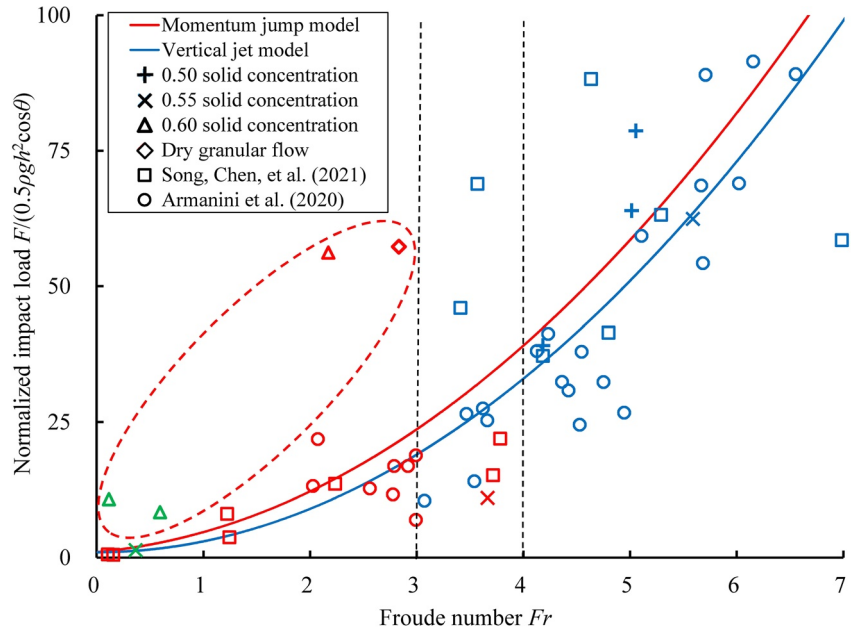


Figure 9. Relationship between frontal impact load and Froude number, based on the hydrostatic approach. Blue denotes the vertical jet mode, red denotes the momentum jump mode, and green denotes the creeping mode.

We further infer the state of static debris from the basal measurement near the barrier (Figure 2b) in Figure 11. Since there is no pore-pressure response for dry granular flows, the state of debris is not regulated by pore pressure (Figure 11a). As expected, the shear stress of the dilute debris flow cannot be maintained and reflects the downstream and upstream movement of the debris (Figure 11d). Moreover, for test 50–100, the pore-fluid pressure follows the normal stress quite well. Once the solid phase settles in the depth direction, the excess pore-fluid pressure is no longer equal to the total stress. This in turn proves that solid-fluid separation does occur.

For test 55–100, as the deposition proceeds, the shear process diminishes. With its solid fraction (0.55) lower than the critical value of 0.58, the granular skeleton finally contracts, and the degree of liquefaction approaches unity (Figure 11c). The shear stress turns to zero, and the state of static debris tends to be a state of liquid ($k_H = 1$). The degree of liquefaction for test 60–100 also increases from 0.18 in the flowing state to 0.59 in the deposit. As a result, the shear stress decreases with increasing normal stress but does not reach zero (Figure 11b). This indicates that the coefficient of earth pressure k_H first approaches the passive state and later decreases with increasing degree of liquefaction.

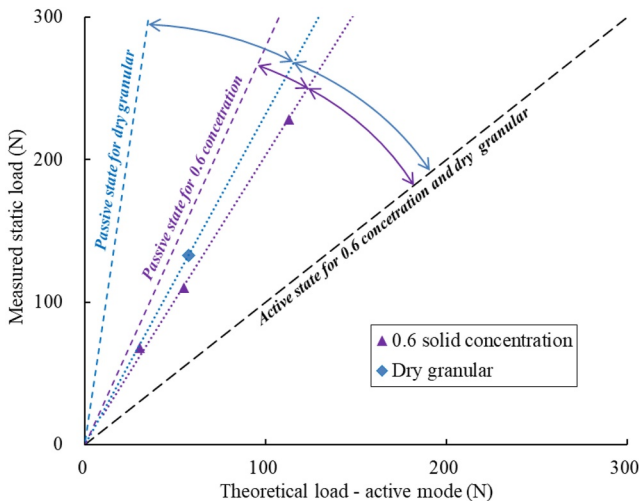


Figure 10. State of the static debris deposit.

6. Phase Diagram for Debris-Flow Impact

With the experimental analysis covering the dilute and dense ranges, we propose a tentative phase diagram for debris-flow impact (Figure 12). Theoretical (i.e., Equations 1 and 4) and experimental studies both reveal the crucial importance of the Froude number on the control of impact dynamics. Two Fr thresholds can be found, and the debris-flow impact can be divided into three phases.

A. Vertical jet mode, $Fr > 3-4$

Above $Fr = 3-4$, the impact process is characterized by a vertical jet (Song, Chen, et al., 2021). Accordingly, the impact load follows the prediction of Equation 1, with $\lambda_{\text{flow}} = 1$ and $k = 1$ forming the lower bound. Because of the high degree of liquefaction and low effective stress, the impact of the dilute debris flow is mainly contributed by the hydrodynamic load. Current dilute debris-flow impact experiments are within this range. Although debris flows with Fr higher than this threshold have been reported, the majority of

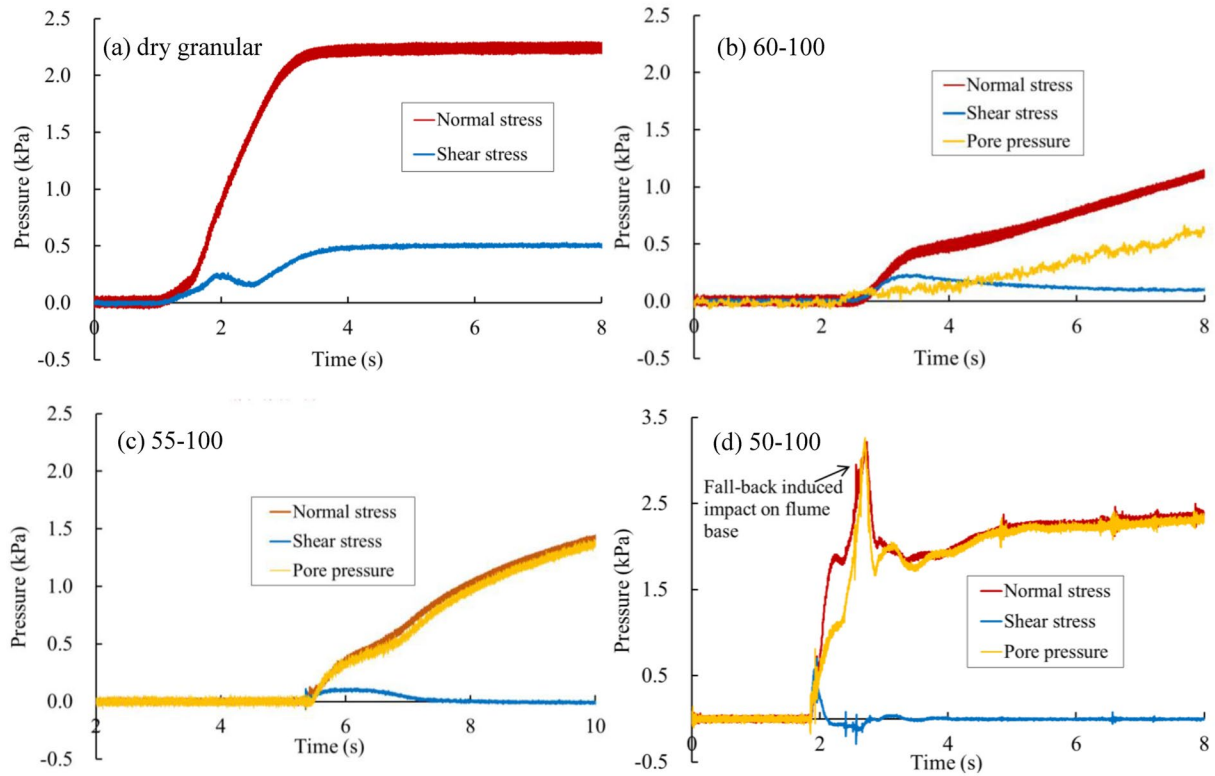


Figure 11. Measured basal normal stress, shear stress, and pore-fluid pressure upon interaction with rigid barrier: (a) dry granular at basal sensing module 3; (b) 60–100 at basal sensing module 3; (c) 55–100 at basal sensing module 1; and (d) 50–100 at basal sensing module 1.

natural debris flows actually lie below this threshold (Hübl et al., 2009). Given the very high Fr for dry granular flow, it would also follow the vertical jet mode. This has been reported by Hákonardóttir et al. (2003).

B. Momentum jump mode, $Fr < 3-4$

Below this threshold, the impact process is characterized by an upstream-moving jump with limited jump height. Accordingly, the impact load follows the prediction of Equation 4, with $\lambda_{\text{flow}} = 1$ and $k = 1$ forming the lower bound. Within this regime, both static and dynamic loads contribute to the overall impact load.

Table 2
Impact Load and Mode of Interaction With Rigid Barrier

Test ID	Froude number Fr	Impact load (N) ^a	Pressure coefficient β based on static approach	Mode	Static load (N)	Deposition height H (m)	Degree of liquefaction for deposits λ_{deposit}
Dry granular	2.83	133.3	57.28	Momentum jump	133.3	0.19	–
60–1	2.17	56.2	12.83	Momentum jump	110.2	0.17	0.57
60–10	0.11	10.8	5.22	Creeping	68.0	0.12	0.48
60–100	0.59	8.4	3.06	Creeping	228.0	0.24	0.59
55–1	5.59	147.9	53.60	Vertical jet	50.5	0.14	0.53
55–10	3.66	19.7	10.96	Momentum jump	38.3	0.11	0.95
55–100	0.36	7.5	1.37	Creeping	57.7	0.14	0.94
50–1	5.02	327.6	63.70	Vertical jet	56.9	0.16	0.94
50–10	5.06	385.0	78.37	Vertical jet	75.2	0.15	0.86
50–100	4.18	161.2	38.98	Vertical jet	69.5	0.16	0.75

^aFor those with a creeping mode (gradual increasing static load), frontal impact loads are adopted for comparison.

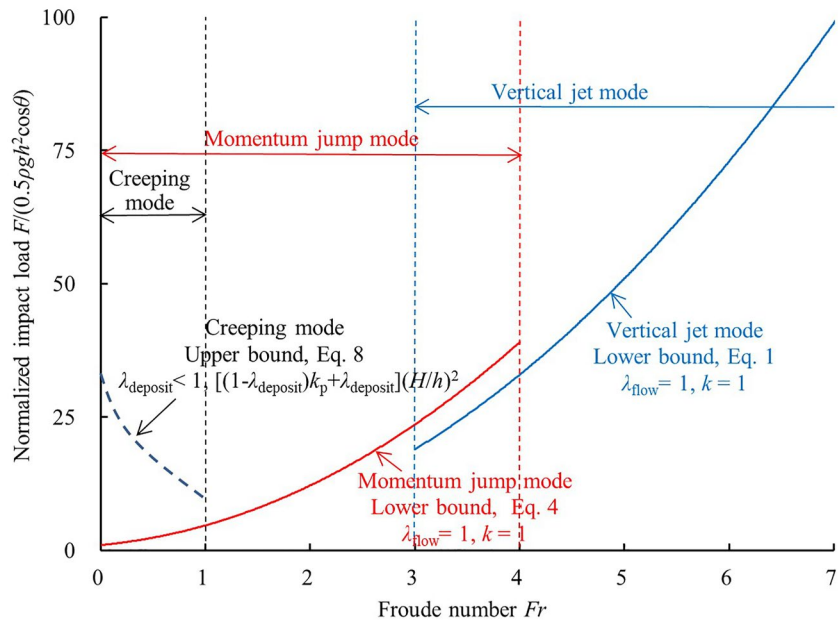


Figure 12. The phase diagram for debris-flow impact on a rigid barrier. The high solid-fraction debris flows are mainly characterized by $Fr < 1$, and the complicated particle-contact stress state renders the impact load undetermined.

C. Creeping mode, $Fr < 1$

Furthermore for $Fr < 1$, the impact process is not violent and is dominated by the static load. However, this regime is rather complicated because most slow-moving dense debris flows are within this range. Due to the creeping (thrust) process of deposition, the state of deposit lies between the at-rest and passive states. Additionally, as revealed in the previous sections, the coefficient of earth pressure varies with the variation in the degree of liquefaction λ_{deposit} . Furthermore, the final deposition height H in the creeping mode could be several times the incoming-flow depth h . In view of the complex state of static debris and final deposition height, the upper bound of the impact load in this regime can be expressed as

$$\begin{aligned} F &= 0.5k_H \rho g H^2 \cos \theta \\ &= 0.5\rho g h^2 \cos \theta [(1 - \lambda_{\text{deposit}})k_p + \lambda_{\text{deposit}}](H/h)^2 \end{aligned} \quad (8)$$

This upper bound is much higher than the prediction using conventional debris-flow impact models (Equations 1 and 4).

Currently, there is still no reliable method for estimating the deposition height H , which is regulated by pore-pressure feedback. Based on the conservation of energy, Faug (2020) proposed an approach for estimating the run-up height and impact load for slow-moving dense flows. However, the strong particle-contact stress indicates a high rate of energy dissipation; therefore, this approach is not applicable to the creeping regime of this study. Note that Fr positively correlates with the degree of liquefaction (Figure 4c), which means that at high Fr , the degree of liquefaction approaches unity. Based on Equation 7, the high degree of liquefaction indicates an earth pressure coefficient k_H close to unity. Therefore, the coefficient of earth pressure k_H within this range ($Fr < 1$) decreases with increasing Fr . A decreasing trend is proposed for the upper bound of the impact load (dashed line in Figure 12).

The proposed phase diagram is not yet complete, with the upper bound in the range $Fr > 1$ undefined. However, since debris flows with $Fr > 1$ are characterized by a high degree of liquefaction, we expect that the theoretical line for predicting the impact load will be unique (i.e., the band between the upper and lower bounds is narrow).

7. Discussion

7.1. Mono-Sized Glass Beads as an Analog Debris-Flow Material

As an analogy of debris material, mono-sized particles could find less chance to fall into the void formed by their neighboring particles. Moreover, compared with well-graded natural debris material, mono-sized particles occupy a larger bulk volume and feature less compressibility. Therefore, a mono-sized granular assembly is more dilative than a well-graded debris material with the same volumetric solid fraction. This explains the negative excess pore pressure observed in this study. From the high degree of liquefaction of USGS large-scale flume tests (Iverson et al., 2010), the excess pore pressures should be positive. This raises a critical question: are the test results with different particle distributions comparable? In this sense, our experimental work with volumetric solid fractions of 60% and 55% clearly reveals the mechanism of dense debris-flow impact but may not be directly comparable with natural debris flows with well-graded particles.

It has been proven that in traditional soil mechanics, under a specific stress state, the distance from the initial solid fraction to the critical-state solid fraction controls the behavior of soil (Been & Jefferies, 1985). For the rheological description of debris-flow behavior, Kostynick et al. (2022) demonstrated that the shear viscosity and yield stress are controlled by the distance from the jamming solid fraction (Boyer et al., 2011). This indicates that the initial volumetric solid fraction is insufficient to describe and compare the debris-flow behavior. Rather, the distance from the initial solid fraction to the critical-state solid fraction $m-m_{\text{crit}}$ is a rational state parameter. Note this state parameter is reflected by Equation 5 of the framework of granular dilatancy in Section 2.2. The effect of the state parameter $m-m_{\text{crit}}$ is further quantified in Section 7.3.

7.2. Timescales in Debris Flow and the Origin of Creeping Behavior

Two pore-pressure processes are involved in debris-flow dynamics. One is the process of pore-pressure generation (positive or negative) by granular dilatancy (contraction or dilation), which relies on the shear-rate distribution (Equations 5 and 6) and thus is categorized as a local effect. Pore-pressure generation occurs along with debris-flow downstream of motion and impact. The other process is the dissipation of the generated disequilibrium pore pressure (global effect). Accordingly, two timescales are involved. Here, we compare the two contrasting timescales of dense debris flows, that is, test 60–100, to elaborate the mechanism of creeping behavior.

One is the timescale for pore-pressure generation, and we adopt the macroscopic timescale of debris motion, t_d , to characterize it

$$t_d = \sqrt{L/g} \quad (9)$$

where L is the length of debris flow (approximately 5 m in this study). The other is the timescale for dissipation of the generated disequilibrium pore pressure along the height (Iverson et al., 2004)

$$t_p = \frac{\eta h^2}{KE} \quad (10)$$

where η is dynamic viscosity of the fluid phase (0.1 Pas for test 60–100); h is flow depth (0.032 m); K is intrinsic permeability of granular material (10^{-10} m² for solid fraction 60% and particle size 0.6 mm); and E is bulk compressive stiffness of granular material with solid fraction 60% ($\sim 10^5$ Pa). The calculated timescale t_p is 10 s, which is one order of magnitude longer than the timescale of pore-pressure generation for test 60–100 ($t_d = 0.7$ s).

Based on the contrast in the order of magnitude, the mechanism of the time-dependent creeping flow and impact behavior is clear. The negative pore pressure generated by shear dilation in dense debris flows (timescale ~ 1 s) cannot be timely equalized through pore pressure dissipation (timescale ~ 10 s). This mechanism is similar to the “viscous” motion of landslides described by Iverson (2005) and could explain many time-dependent behaviors of dense debris flows.

7.3. Scale Effect

Small-scale flume tests are still widely adopted for investigating the mechanisms of debris flows since controlled large-scale tests are costly. For the potential applicability of these findings to real-scale hazards, it is essential to discuss the scale effect. We explore the scale effect at two levels. At the macroscopic level, as shear dilation/contraction results in drastic differences in mobility and impact behavior, the distance from the initial solid

Table 3
Typical Values of the Dimensionless Numbers

Test ID	$m-m_{\text{crit}}$	N_p^a	N_R	N_S	N_B
60–1	0.02	4.2×10^0	5.6×10^5	4.6×10^{-3}	7.3×10^1
60–10	0.02	9.1×10^{-1}	3.9×10^4	1.5×10^{-5}	4.2×10^{-1}
60–100	0.02	7.0×10^{-2}	4.5×10^3	4.1×10^{-4}	2.0×10^{-1}
55–1	–0.03	1.4×10^1	3.8×10^5	1.4×10^{-1}	2.0×10^2
55–10	–0.03	2.0×10^0	3.4×10^4	1.1×10^{-1}	1.3×10^1
55–100	–0.03	6.5×10^{-2}	5.9×10^3	6.5×10^{-4}	9.2×10^{-2}
50–1	–0.08	4.4×10^0	5.5×10^5	1.0×10^{-1}	1.1×10^2
50–10	–0.08	4.8×10^{-1}	5.5×10^4	3.3×10^{-1}	1.2×10^1
50–100	–0.08	5.8×10^{-2}	5.1×10^3	9.9×10^{-2}	9.1×10^{-1}
Dense debris-flow mobilization ^b	0.03	2×10^{-3}	2×10^6	–	–
Loose debris-flow mobilization ^b	–0.08	5×10^{-3}	2×10^6	–	–
Gate-release of debris flow ^c	–0.02	2×10^{-4}	1×10^5	1.0×10^{-1}	6×10^2

^aEstimation of the bulk compressive stiffness E for suspended particles could have an error of one order of magnitude. ^bFrom George and Iverson (2014). ^cFrom Iverson et al. (2010).

fraction to the critical-state solid fraction $m-m_{\text{crit}}$ is a governing index. As discussed in Section 7.1, this index serves as a reference for debris flows with varying compositions to compare with each other. With pore-pressure feedback as a key focus, the comparison between the timescale of debris-flow motion (pore-pressure generation) and the timescale of disequilibrium pore-pressure dissipation reveals whether excess pore pressure could be maintained (Iverson et al., 2004)

$$N_p = \frac{\sqrt{L/g}}{\eta h^2 / KE} \quad (11)$$

The definitions of the parameters are detailed in Section 7.2; bulk compressive stiffnesses E of 10^5 , 5×10^4 , and 10^4 Pa are adopted for 60%, 55%, and 50% solid fractions, respectively. The Reynolds number quantifies the relative importance between flow inertia and viscous force (Iverson et al., 2004)

$$N_R = \frac{\rho h \sqrt{gL}}{\eta} \quad (12)$$

At the grain scale, we explore the relative importance between particle-collision, particle-contact friction, and fluid-viscous stresses. The Savage number N_S (particle collision vs. particle-contact friction) and Bagnold number N_B (particle collision vs. fluid-viscous stress) are adopted

$$N_S = \frac{\rho_s \dot{\gamma}^2 \delta^2}{\sigma - p} \quad (13)$$

$$N_B = \left[\frac{m}{1-m} \right] \frac{\rho_s \dot{\gamma} \delta^2}{\eta} \quad (14)$$

Typical values of the above dimensionless numbers are summarized in Table 3. USGS large-scale flume tests are also included for comparison. Specifically, we adopt the two tests of the onset of debris-flow motion (further simulated by D-Claw by George & Iverson, 2014), with one being densely packed and the other being loosely packed. The state parameter $m-m_{\text{crit}}$ of these two tests is comparable with the 60% solid-fraction test, that is, on the dilative side of the solid fraction ($m-m_{\text{crit}} > 0$). Furthermore, the tests of debris-flow dynamics by Iverson et al. (2010) are adopted for comparison with 55% and 50% solid-fraction tests since they are all on the contractive side of the solid fraction ($m-m_{\text{crit}} < 0$).

With increasing fluid viscosity from 0.001 to 0.1 Pas, N_p is reduced by two orders of magnitude. With a longer drainage path h (an indication of scale for debris flow), N_p of the USGS flume tests is 1–2 orders of magnitude lower than that of this study (Figure 13a). A much lower N_p indicates that it takes much longer time for

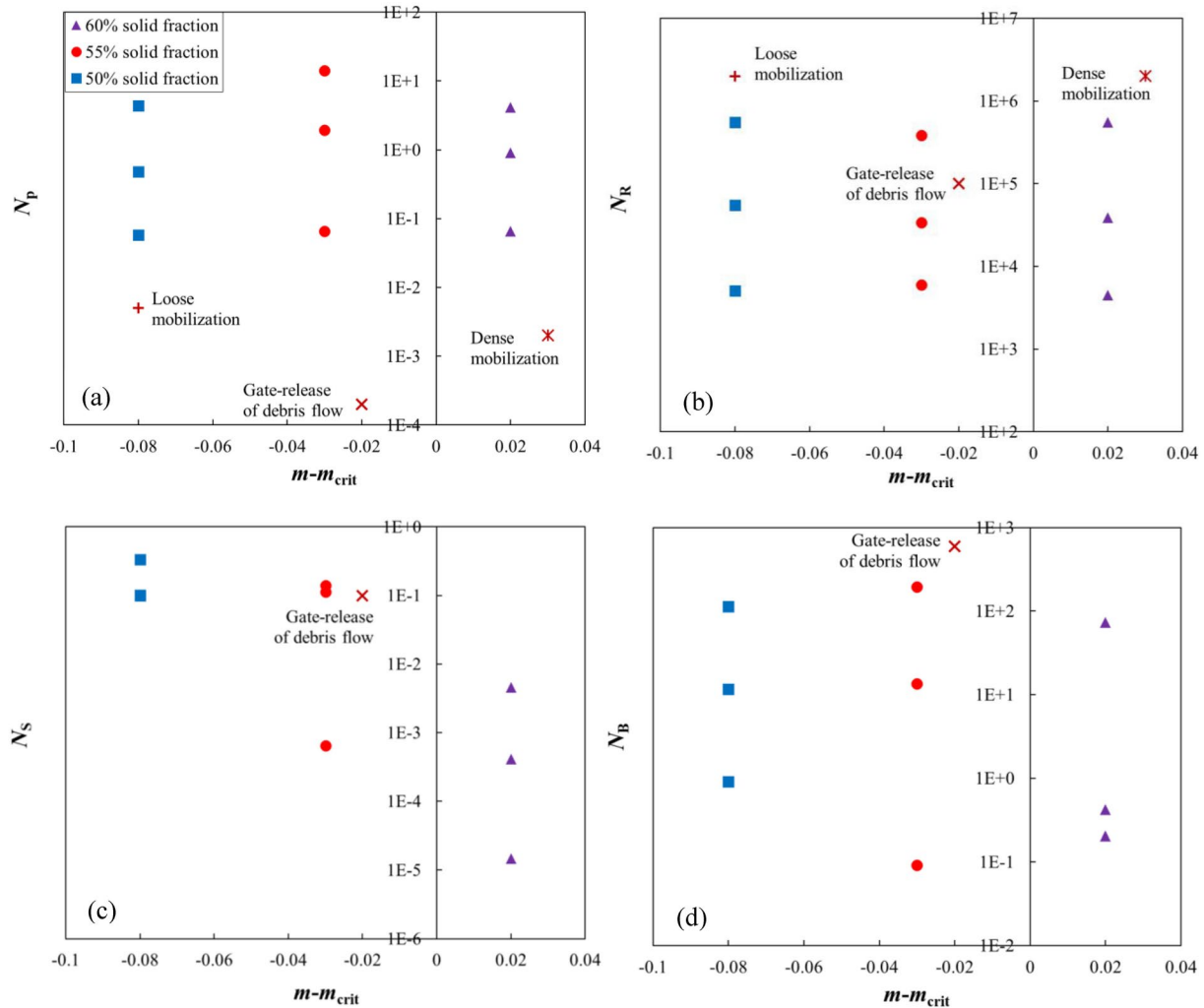


Figure 13. Scale effect reflected by the dimensionless number (a) N_p , (b) N_R , (c) N_S , and (d) N_B . Data from George and Iverson (2014) and Iverson et al. (2010) are shown for comparison.

pore-pressure dissipation on the real scale. In other words, with the same $m-m_{crit}$ for small-scale and real-scale debris flows, the dilute (contractive) flow is more fluid-like at the real scale, while the dense (dilative) flow exhibits more creeping at the real scale.

N_R and N_B quantify the macroscopic and grain-scale inertial force to fluid-viscous force, respectively. For the large-scale tests, the inertial force dominates over the viscous force (Figures 13b and 13d). N_S is a function of the state parameter $m-m_{crit}$ (Figure 13c), and the small-scale flume tests generally match the large-scale tests. For dense flows ($m-m_{crit} > 0$), granular dilation enhances the particle-contact effective stress, thus the frictional force dominates. With decreasing solid fraction, the particle-collision stress tends to dominate. The state parameter $m-m_{crit}$ controls the dilative or contractive behavior of debris flows, and thus is a primary index for the design of debris-flow experiments.

Except for N_S , a difference (scale effect) is found in the timescale of pore-pressure dissipation and inertial-viscous forces. Additional scaled data of dense debris flows, either from large-scale flumes or field monitoring, are instrumental in strengthening the proposed phase diagram.

8. Conclusions

From a geotechnical viewpoint, the complexity of dense-flow impact dynamics originates from the state of the solid phase, especially regulated by the feedback between granular dilatancy and the pore-pressure response.

Reliable measurements of the stress state and pore pressure of dense and dilute debris flows were carried out in this study. For the first time, in a debris-flow impact study, the regulation of pore-pressure feedback on the impact behavior is revealed. Key conclusions may be drawn as follows.

- (a) With a special focus on dense debris flows, the negative correlation between excess pore pressure and granular dilatancy is confirmed. We further elaborate that the initial volumetric solid fraction is insufficient for describing debris-flow behavior. Rather, the distance from the initial volumetric solid fraction to the critical-state solid fraction is a rational state parameter.
- (b) A creeping mode is found for the slow-moving dense-flow impact, which is regulated by the pore-pressure evolution. Remarkable arching effects on the barrier are observed for flows with nonnegligible particle-contact friction. The stability of granular arches is a function of the degree of liquefaction. As the degree of liquefaction approaches unity (liquefied), the granular arches are eliminated.
- (c) The time-dependent creeping impact behavior is further elaborated through the involved timescales. By adopting the parameters of dense flows, the contrast between the calculated timescale for the diffusion of disequilibrium pore pressure and the timescale for pore pressure generation further confirms that the macroscopic creeping impact behavior is a result of the untimely response of pore pressure to granular dilatancy.
- (d) A passive state of granular material is observed in the frontal impact as well as in the final deposit of dense debris flows. The passive state, as well as granular arching, is a result of sustained particle-contact friction and reflects the interaction history of dense debris flows against obstacles. For dilute debris flows, instant particle collision and a high degree of liquefaction facilitate an isotropic stress state, with no stress history recorded in the deposit. As a result of the passive state, the impact load of dense debris flows cannot be conservatively estimated by fast-moving dilute debris-flow load models.
- (e) A tentative phase diagram is proposed for dense and dilute debris-flow impact. Above the threshold $Fr = 3-4$, the impact obeys the vertical jet mode, and the hydrodynamic force dominates the total impact load. Below threshold $Fr = 3-4$, the impact obeys the momentum jump mode, and both hydrodynamic and static forces contribute to the total impact load. Furthermore, for dense debris flows with $Fr < 1$, the passive stress state, degree of liquefaction, and deposition height together determine the upper bound of the impact load.

Conflict of Interest

The authors declare no conflicts of interest relevant to this study.

Data Availability Statement

The data set (Song, 2023, <https://doi.org/10.12380/Debris.msdc.000009>) in this paper is available in the Mountain Science Data Center via <http://www.msdc.ac.cn/#/>, with registration.

Acknowledgments

The authors acknowledge the financial supports from the National Natural Science Foundation of China (Grants 42077256 and 41925030), the Second Tibetan Plateau Scientific Expedition and Research Program (STEP, Grant 2019OZKK0904), and the Science and Technology Research Program of Institute of Mountain Hazards and Environment, Chinese Academy of Sciences (Grant IMHE-CXTD-02). Support from the Dongchuan Debris Flow Observation and Research Station (DDFORS) of Chinese Academy of Sciences is acknowledged.

References

- Albaba, A., Lambert, S., & Faug, T. (2018). Dry granular avalanche impact force on a rigid wall: Analytic shock solution versus discrete element simulations. *Physical Review E*, 97(5), 052903. <https://doi.org/10.1103/PhysRevE.97.052903>
- Amarsid, L., Delenne, J. Y., Mutabaruka, P., Monerie, Y., Perales, F., & Radjai, F. (2017). Viscoinertial regime of immersed granular flows. *Physical Review E*, 96(1), 012901. <https://doi.org/10.1103/PhysRevE.96.012901>
- Armanini, A., Rossi, G., & Larcher, M. (2020). Dynamic impact of a water and sediments surge against a rigid wall. *Journal of Hydraulic Research*, 58(2), 314–325. <https://doi.org/10.1080/00221686.2019.1579113>
- ASI. (2011). *ONR 24802: Protection works for torrent control—Design of structures*. Austrian Standards Institute.
- ASI. (2013). *ONR 24801: Protection works for torrent control—Static and dynamic actions on structures*. Austrian Standards Institute.
- Been, K., & Jefferies, M. G. (1985). A state parameter for sands. *Géotechnique*, 35(2), 99–112. <https://doi.org/10.1680/geot.1985.35.2.99>
- Bowman, E. T., Laue, J., Imre, B., & Springman, S. M. (2010). Experimental modelling of debris flow behaviour using a geotechnical centrifuge. *Canadian Geotechnical Journal*, 47(7), 742–762. <https://doi.org/10.1139/t09-141>
- Boyer, F., Guazzelli, É., & Pouliquen, O. (2011). Unifying suspension and granular rheology. *Physical Review Letters*, 107(18), 188301. <https://doi.org/10.1103/PhysRevLett.107.188301>
- CAGHP. (2018). *T/CAGHP 021-2018: Specification of design of debris flow prevention*. China Association of Geological Hazard Prevention (CAGHP). (in Chinese).
- Cassar, C., Nicolas, M., & Pouliquen, O. (2005). Submarine granular flows down inclined planes. *Physics of Fluids*, 17(10). <https://doi.org/10.1063/1.2069864>
- Chanson, H. (2004). 14—Physical modelling of hydraulics. In H. Chanson (Ed.), *Hydraulics of open channel flow* (2nd ed., pp. 253–274). Butterworth-Heinemann. <https://doi.org/10.1016/B978-075065978-9/50021-0>
- Chen, Q., Song, D., Chen, X., & Zhong, W. (2023). Visco-collisional scaling law of flow resistance and its application in debris-flow mobility. *Journal of Geophysical Research: Earth Surface*, 128(2), e2022JF006712. <https://doi.org/10.1029/2022JF006712>

- Courrech du Pont, S., Gondret, P., Perrin, B., & Rabaud, M. (2003). Granular avalanches in fluids. *Physical Review Letters*, *90*(4), 044301. <https://doi.org/10.1103/PhysRevLett.90.044301>
- Fang, J., Wang, L., Hong, Y., & Zhao, J. (2022). Influence of solid–fluid interaction on impact dynamics against rigid barrier: CFD–DEM modeling. *Géotechnique*, *72*(5), 391–406. <https://doi.org/10.1680/jgeot.19.P.160>
- Faug, T. (2015). Macroscopic force experienced by extended objects in granular flows over a very broad Froude-number range: Macroscopic granular force on extended object. *European Physical Journal E: Soft Matter*, *38*(5), 120. <https://doi.org/10.1140/epjef/2015-15034-3>
- Faug, T. (2020). Impact force of granular flows on walls normal to the bottom: Slow versus fast impact dynamics. *Canadian Geotechnical Journal*, *58*(1), 114–124. <https://doi.org/10.1139/cgj-2019-0399>
- GEO. (2020). *Enhanced technical guidance on design of rigid debris-resisting barriers*. GEO Technical Guidance Note No. 52. Geotechnical Engineering Office (GEO).
- George, D., & Iverson, R. M. (2014). A depth-averaged debris-flow model that includes the effects of evolving dilatancy. II. Numerical predictions and experimental tests. *Proceedings of the Royal Society A: Mathematical, Physical and Engineering Sciences*, *470*(2170), 20130820. <https://doi.org/10.1098/rspa.2013.0820>
- Gravish, N., & Goldman, D. (2014). Effect of volume fraction on granular avalanche dynamics. *Physical Review E: Statistical, Nonlinear, and Soft Matter Physics*, *90*(3), 032202. <https://doi.org/10.1103/PhysRevE.90.032202>
- Guazzelli, É., & Pouliquen, O. (2018). Rheology of dense granular suspensions. *Journal of Fluid Mechanics*, *852*, P1. <https://doi.org/10.1017/jfm.2018.548>
- Hákonardóttir, K. M., Hogg, A. J., Batey, J., & Woods, A. W. (2003). Flying avalanches. *Geophysical Research Letters*, *30*(23), 2191. <https://doi.org/10.1029/2003GL018172>
- Hu, K., Wei, F., & Li, Y. (2011). Real-time measurement and preliminary analysis of debris-flow impact force at Jiangjia Ravine, China. *Earth Surface Processes and Landforms*, *36*(9), 1268–1278. <https://doi.org/10.1002/esp.2155>
- Hübl, J., Suda, J., Proske, D., Kaitna, R., & Scheidl, C. (2009). Debris flow impact estimation. In *Paper presented at proceedings of the 11th international symposium on water management and hydraulic engineering*. University of Ss Cyril and Methodius, Faculty of Civil Engineering.
- Hungr, O., Leroueil, S., & Picarelli, L. (2014). The Varnes classification of landslide types, an update. *Landslides*, *11*(2), 167–194. <https://doi.org/10.1007/s10346-013-0436-y>
- Hungr, O., Morgan, G. C., & Kellerhals, R. (1984). Quantitative analysis of debris torrent hazards for design of remedial measures. *Canadian Geotechnical Journal*, *21*(4), 663–677. <https://doi.org/10.1139/t84-073>
- Iverson, R. M. (2005). Regulation of landslide motion by dilatancy and pore pressure feedback. *Journal of Geophysical Research*, *110*(F2), F02015. <https://doi.org/10.1029/2004JF000268>
- Iverson, R. M., & George, D. (2014). A depth-averaged debris-flow model that includes the effects of evolving dilatancy. I. Physical basis. *Proceedings of the Royal Society A: Mathematical, Physical and Engineering Sciences*, *470*(2170), 20130819. <https://doi.org/10.1098/rspa.2013.0819>
- Iverson, R. M., & George, D. (2019). Basal stress equations for granular debris masses on smooth or discretized slopes. *Journal of Geophysical Research: Earth Surface*, *124*(6), 1464–1484. <https://doi.org/10.1029/2018JF004802>
- Iverson, R. M., Logan, M., & Denlinger, R. (2004). Granular avalanches across irregular three-dimensional terrain: 2. Experimental tests. *Journal of Geophysical Research*, *109*(F1), F01015. <https://doi.org/10.1029/2003JF000084>
- Iverson, R. M., Logan, M., Lahusen, R., & Berti, M. (2010). The perfect debris flow? Aggregated results from 28 large-scale experiments. *Journal of Geophysical Research*, *115*(F3), F03005. <https://doi.org/10.1029/2009JF001514>
- Iverson, R. M., Reid, M. E., & Lahusen, R. (1997). Debris-flow mobilization from landslides. *Annual Review of Earth and Planetary Sciences*, *25*(1), 85–138. <https://doi.org/10.1146/annurev.earth.25.1.85>
- Johnson, C., Kokelaar, P., Iverson, R., Logan, M., Lahusen, R., & Gray, J. (2012). Grain-size segregation and levee formation in geophysical mass flows. *Journal of Geophysical Research*, *117*(F1), 1032. <https://doi.org/10.1029/2011JF002185>
- Jop, P., Forterre, Y., & Pouliquen, O. (2005). Crucial role of sidewalls in granular surface flows: Consequences for the rheology. *Journal of Fluid Mechanics*, *541*(-1), 167–192. <https://doi.org/10.1017/S0022212005005987>
- Kong, Y., Guan, M., Li, X., Zhao, J., & Yan, H. (2022a). Bi-linear laws govern the impacts of debris flows, debris avalanches, and rock avalanches on flexible barrier. *Journal of Geophysical Research: Earth Surface*, *127*(11), e2022JF006870. <https://doi.org/10.1029/2022JF006870>
- Kong, Y., Guan, M., Li, X., Zhao, J., & Yan, H. (2022b). How flexible, slit and rigid barriers mitigate two-phase geophysical mass flows: A numerical appraisal. *Journal of Geophysical Research: Earth Surface*, *127*(6), e2021JF006587. <https://doi.org/10.1029/2021JF006587>
- Kostynick, R., Matinpour, H., Pradeep, S., Haber, S., Sauret, A., Meiburg, E., et al. (2022). Rheology of debris flow materials is controlled by the distance from jamming. *Proceedings of the National Academy of Sciences of the United States of America*, *119*(44). <https://doi.org/10.1073/pnas.2209109119>
- Kwan, J. S. H. (2012). Supplementary technical guidance on design of rigid debris-resisting barriers. GEO Report No. 270. Geotechnical Engineering Office, HKSAR Government.
- Kyburz, M. L., Sovilla, B., Gaume, J., & Ancey, C. (2022). Physics-based estimates of drag coefficients for the impact pressure calculation of dense snow avalanches. *Engineering Structures*, *254*, 113478. <https://doi.org/10.1016/j.engstruct.2021.113478>
- Liu, D., You, Y., Liu, J., Li, Y., Zhang, G., & Wang, D. (2019). Spatial-temporal distribution of debris flow impact pressure on rigid barrier. *Journal of Mountain Science*, *16*(4), 793–805. <https://doi.org/10.1007/s11629-018-5316-4>
- Nagl, G., Hübl, J., & Kaitna, R. (2022). Stress anisotropy in natural debris flows during impacting a monitoring structure. *Landslides*, *19*(1), 211–220. <https://doi.org/10.1007/s10346-021-01779-2>
- Ng, C. W. W., Haiming, L., Choi, C., Kwan, J., & Pun, W. (2021). Impact dynamics of boulder-enriched debris flow on a rigid barrier. *Journal of Geotechnical and Geoenvironmental Engineering*, *147*(3), 04021004. [https://doi.org/10.1061/\(ASCE\)GT.1943-5606.0002485](https://doi.org/10.1061/(ASCE)GT.1943-5606.0002485)
- NILIM. (2016a). *Manual of technical standard for designing Sabo facilities against debris flow and driftwood*. Technical Note of NILIM No. 905. Natural Institute for Land and Infrastructure Management (NILIM). (in Japanese).
- NILIM. (2016b). *Manual of technical standard for establishing Sabo master plan for debris flow and driftwood*. Technical Note of NILIM No. 904. Natural Institute for Land and Infrastructure Management (NILIM). (in Japanese).
- Pailha, M., Nicolas, M., & Pouliquen, O. (2008). Initiation of underwater granular avalanches: Influence of the initial volume fraction. *Physics of Fluids*, *20*(11). <https://doi.org/10.1063/1.3013896>
- Pierson, T. C. (2005). Hyperconcentrated flow—Transitional process between water flow and debris flow. In M. Jakob, & O. Hungr (Eds.), *Debris-flow hazards and related phenomena* (pp. 159–202). Springer Berlin Heidelberg. https://doi.org/10.1007/3-540-27129-5_8
- Salm, B. (1967). On nonuniform, steady flow of avalanching snow. In *Assemblée générale de berne, publication No. 79*. IAHS Wallingford Oxfordshire U.K.

- Sanvitale, N., & Bowman, E. T. (2016). Using PIV to measure granular temperature in saturated unsteady polydisperse granular flows. *Granular Matter*, 18(3), 57. <https://doi.org/10.1007/s10035-016-0620-6>
- Scheidl, C., Chiari, M., Kaitna, R., Müllegger, M., Krawtschuk, A., Zimmermann, T., & Proske, D. (2013). Analysing debris-flow impact models, based on a small scale modelling approach. *Surveys in Geophysics*, 34(1), 121–140. <https://doi.org/10.1007/s10712-012-9199-6>
- Song, D. (2023). Dataset of dilute and dense debris flow impact against rigid obstacle in an experimental flume [Dataset]. Mountain Science Data Center. <https://doi.org/10.12380/Debri.msdc.000009>
- Song, D., Bai, Y. T., Chen, X. Q., Choi, C. E., Pasuto, A., & Peng, P. (2022). Assessment of debris flow multiple-surge load model based on the physical process of debris-barrier interaction. *Landslides*, 19(5), 1165–1177. <https://doi.org/10.1007/s10346-021-01778-3>
- Song, D., Chen, X. Q., Zhou, G. G. D., Lu, X. Q., Cheng, G. W., & Chen, Q. (2021). Impact dynamics of debris flow against rigid obstacle in laboratory experiments. *Engineering Geology*, 291, 106211. <https://doi.org/10.1016/j.enggeo.2021.106211>
- Song, D., Choi, C. E., Ng, C. W. W., & Zhou, G. G. D. (2018). Geophysical flows impacting a flexible barrier: Effects of solid-fluid interaction. *Landslides*, 15(1), 99–110. <https://doi.org/10.1007/s10346-017-0856-1>
- Song, D., Zhou, G. G. D., & Chen, Q. (2021). Flow resistance in the transition from dense to dilute granular-fluid flows. *Granular Matter*, 23(3), 73. <https://doi.org/10.1007/s10035-021-01134-1>
- Sovilla, B., Kern, M., & Schaer, M. (2010). Slow drag in wet-snow avalanche flow. *Journal of Glaciology*, 56(198), 587–592. <https://doi.org/10.3189/002214310793146287>
- Vagnon, F., & Segalini, A. (2016). Debris flow impact estimation on a rigid barrier. *Natural Hazards and Earth System Sciences*, 16(7), 1691–1697. <https://doi.org/10.5194/nhess-16-1691-2016>
- Voellmy, A. (1955). Über die Zerstörungskraft von Lawinen. *Schweizerische Bauzeitung*, 73, 159–165.
- Wood, D. M. (1990). *Soil behaviour and critical state soil mechanics*. Cambridge University Press. <https://doi.org/10.1017/CBO9781139878272>
- Zanuttigh, B., & Lamberti, A. (2006). Experimental analysis of the impact of dry avalanches on structures and implication for debris flows. *Journal of Hydraulic Research*, 44(4), 522–534. <https://doi.org/10.1080/00221686.2006.9521703>